ACS Energy LETTERS

http://pubs.acs.org/journal/aelccp

Designing the Perovskite Structural Landscape for Efficient Blue Emission

Natalia Yantara,+ Nur Fadilah Jamaludin,+ Benny Febriansyah, David Giovanni, Annalisa Bruno, Cesare Soci, Tze Chien Sum, Subodh Mhaisalkar,* and Nripan Mathews*

Cite This: *ACS Energy Lett.* 2020, 5, 1593−1600

Read Online

ACCESS | Metrics & More | Article Recommendations | Supporting Information

ABSTRACT: Despite the rapid development of perovskite light-emitting diodes (PeLEDs) in recent years, blue PeLEDs' efficiencies are still inferior to those of their red and green counterparts. The poor performance is associated with, among other factors, halide segregation in bromide-chloride materials and energy funneling to lowest bandgaps in multilayered Ruddlesden−Popper (RP) systems. This study reports that compositional engineering through prudent selection of the A-site cation in a pure bromide RP system can result in a narrow distribution of layered domains. With a narrow distribution centered around the desired RP domain, efficient energy cascade to yield blue emission is ensured. Coupled with rapid nucleation induced by an antisolvent deposition technique, record efficiencies of 2.34 and 5.08%, corresponding to color-stable deep blue (∼465 nm) and cyan (∼493 nm), respectively, were attained. This composition and process engineering to design favorable structural landscape is transferrable to other material systems, which paves the way for high-performance PeLEDs.

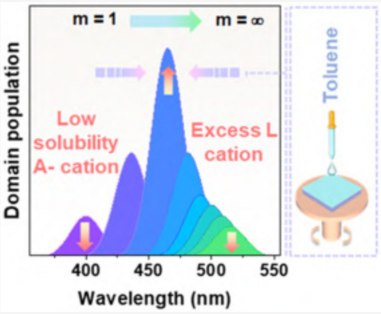

Halide compounds with ABX_3 perovskite structure (where A, B, and X are monovalent cation, divalent cation and halide anion respectively) are attractive for optoelectronic research owing to their unique properties such as long carrier diffusion lengths,[1−3] low trap densities,[4] tunable bandgaps,[5] and high luminescence quantum yields.[6] Within five years, rapid progress in perovskite-based light-emitting diodes (PeLEDs) research drove the efficiency increase from <1%[7] to 20%.[8,9] Nevertheless, the efficiency strides have been noted only for green and red emissions, with the efficiency for blue-emitting PeLEDs still wanting. Although wide bandgap perovskites are achievable by employing chloride, the penchant for deep trap state formation increases nonradiative recombination.[10] Attempts to yield blue emission through partial bromide substitution are afflicted with color instability and low efficiency due to reduced photoluminescence quantum yield (PLQY) and electric field-induced halide segregation.[11] Therefore, it is imperative that an alternative strategy be devised to obtain spectrally stable blue PeLEDs (bandgap, $E_g \geq 2.48{-}2.56$ eV).

Another approach involves the substitution of A-site cation with spacer molecules (L) resulting in the formation of Ruddlesden−Popper (RP) perovskites with reduced $[BX_6]$ octahedral network connectivity.[12] Upon introducing monovalent ammonium molecules, layered RP perovskite with chemical formula $L_2A_{m-1}B_mX_{3m+1}$ is produced, depending on the degree of L cation incorporation into the crystal structure (m). While E_g can be widened by decreasing the number of m layers,[13] incorporating more insulating L cations would impede carrier transport.[14] This underscores the need for emissive perovskite layers consisting of an intermediate number of m layers to satisfy both E_g and charge transport criteria. However, depositing phase-pure $m \geq 2$ films is a challenge because of (1) the progressively smaller difference in thermodynamic stability of phases with increasing number of m layers and/or (2) the propensity for $m = 1$ formation due to strong van der Waals interactions between L−L cations, which will deplete the concentration of L cations in the reservoir and thus encourage formation of heterogeneous films.[15] Formation of a mixed-dimensional RP perovskite film promotes energy transfer to the smallest E_g domains which facilitates the fabrication of high-efficiency PeLEDs.[16,17] Conversely, efficient energy cascade from high-E_g domains (donor) to low-E_g domains (acceptor) reveals the need to eliminate formation of $m \approx \infty$ domains to achieve color-pure blue-emitting RP perovskite.

Previous reports have shown that excess L cation is needed to tailor the m domain distribution. For example, a complex 4-cation system can be employed to control the m domain distribution which results in PeLED with external quantum

Received: March 11, 2020
Accepted: April 15, 2020
Published: April 15, 2020

https://dx.doi.org/10.1021/acsenergylett.0c00559

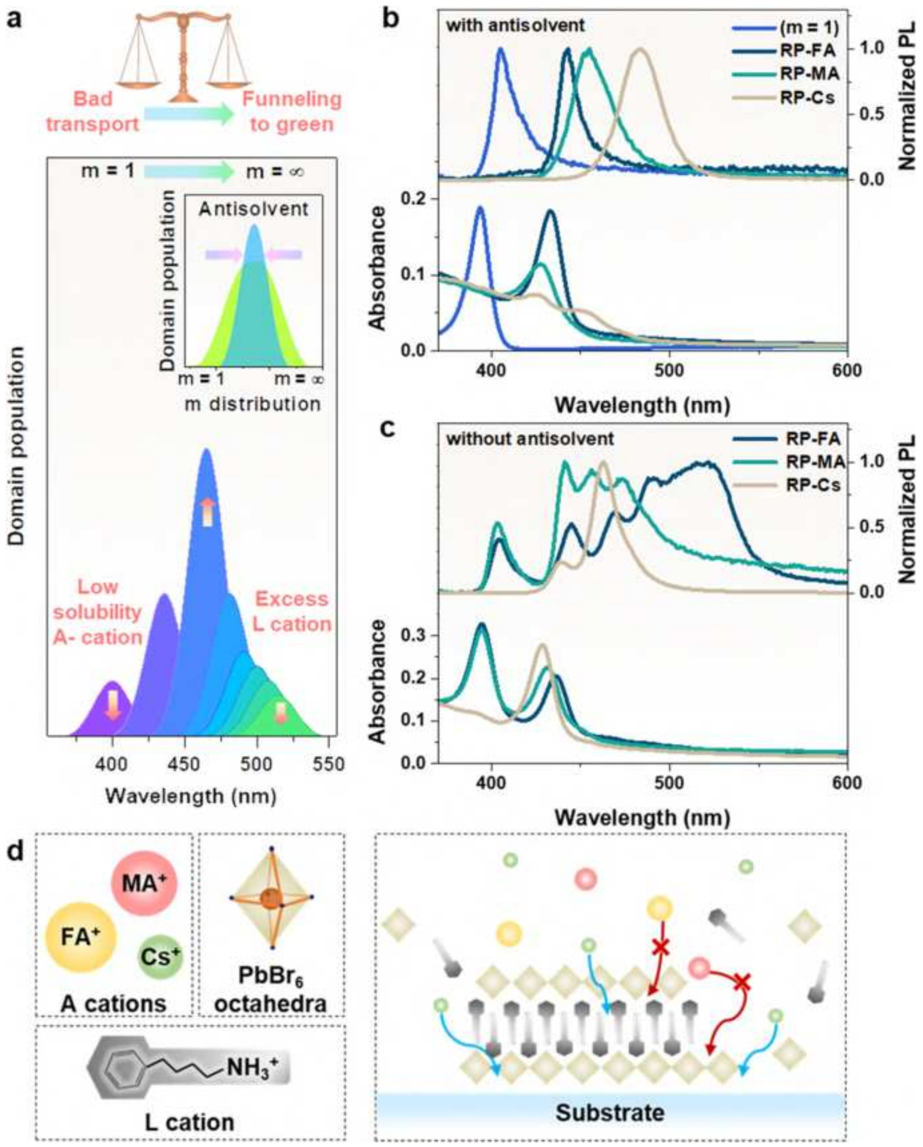

Figure 1. Strategy and mechanism to create pure blue emissive RP perovskite ($L_2A_{m-1}B_mX_{3m+1}$ with m corresponding to the degree of L cation incorporation). Schematic diagram representing the strategy adopted to form intermediate m domains for blue emissive RP films with PBA^+ as L cation, where increasing concentration of low-solubility A cation and introducing excess L cation in the perovskite precursor solution suppresses the formation of $m = 1$ and $m = \infty$ domains (a). Inset of panel (a) illustrates the effect of antisolvent treatment on m domain distribution. The absorbance and normalized photoluminescence spectra of PBA_2PbBr_4 ($m = 1$) and RP films prepared from $\langle m \rangle = 2$ solutions with different A-site cations with (b) and without (c) antisolvent indicate that m domain distribution can be narrowed by employing both low-solubility A-site cation and antisolvent treatment. The schematic diagram of proposed RP formation mechanism highlighting the formation of intermediate m domains by the favorable incorporation of small sized and low-solubility A-site cation (Cs^+) into $m = 1$ system (d).

efficiency (EQE) of 1.5% at 490 nm electroluminescence (EL) peak emission.[15] A triple-cation strategy where RP perovskite alloyed with Rb is coupled with in situ passivation has enabled PeLEDs with EQE of 1.35% at 475 nm peak emission[18] to be produced. Recently, another triple-cation approach to form nanoparticles within RP phases yielding EQE of 9.5% at 483 nm peak emission was reported.[19] Despite the high efficiency, the lack of in-depth study on the crystallization kinetics of RP perovskite highlights the need for a more systematic study on cation interactions.

Here, the crystallization kinetics of RP perovskite is assessed, allowing for tailoring of narrow and intermediate m domains through compositional engineering of simple bicationic systems. We postulate that by introducing excess L cation together with a low-solubility A-site cation to promote fast nucleation, a narrow, monodispersed distribution of intermediate m domains centered at the desired blue emission peak can be attained. In conjunction, process engineering to induce fast nucleation further reduces the m domain distribution. Those strategies enable us to achieve efficient and spectrally stable PeLEDs spanning the entire blue region with EQEs of 2.34%, 4.34%, and 5.08% at EL peak wavelengths of 465, 486, and 493 nm, respectively. The applicability of this concept to other L cation systems showcases the broader impact of this study toward the development of efficient PeLEDs.

To obtain intermediate m domains, $m = 1$ domain formation is suppressed by employing low-solubility bromide salt to boost the incorporation of A-site cation, whereas excess L

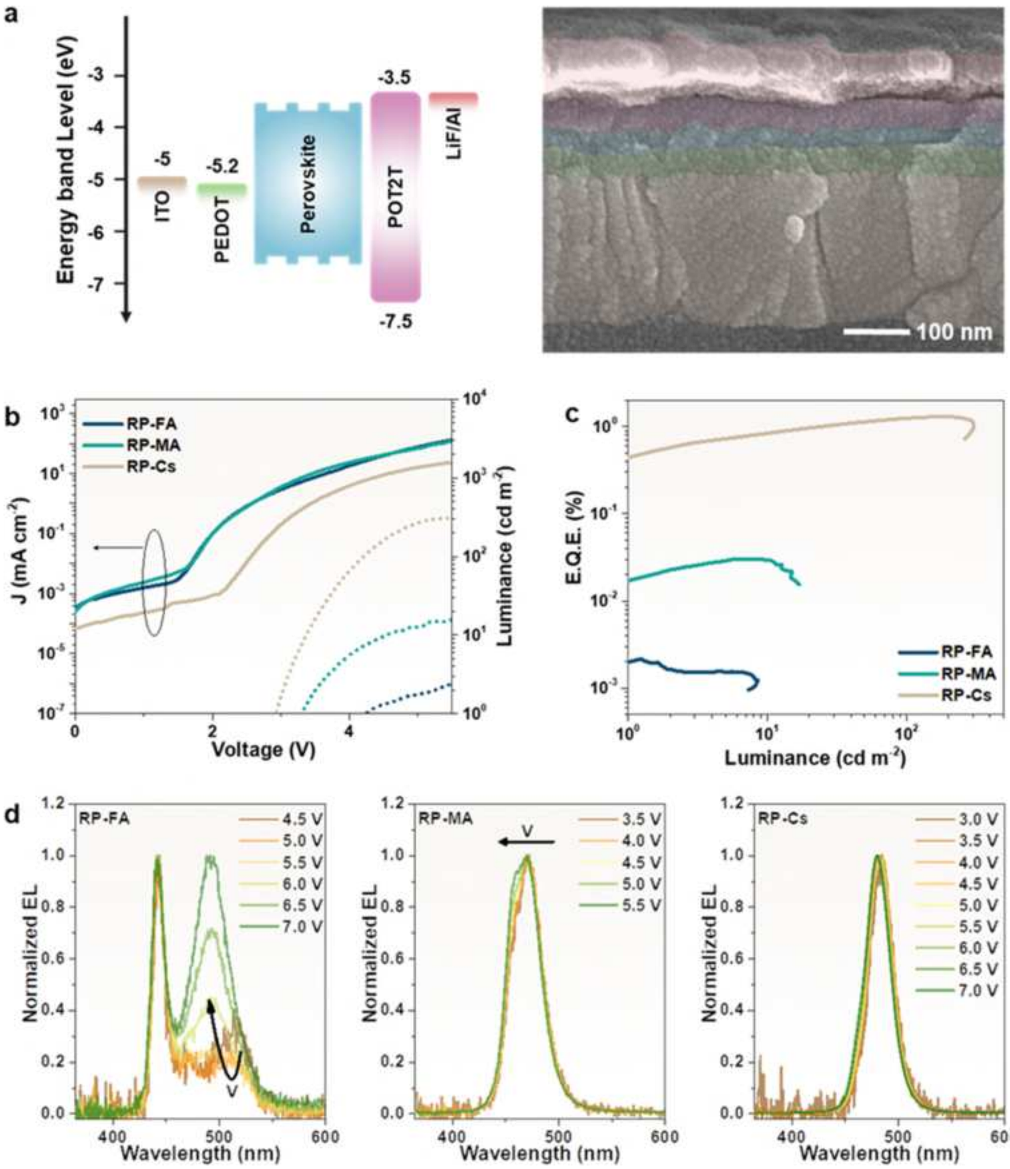

Figure 2. Electrical and optical characteristics of RP-based PeLEDs. Energy band alignment of the different layers in the device stack together with the corresponding cross-sectional image (a). The current density (*J*) and luminance response as a function of voltage (b), the EQE versus luminance (c) for devices deposited from ⟨*m*⟩ = 2 precursor solutions of RP-FA, RP-MA, and RP-Cs. The corresponding normalized EL spectra at various applied bias (d) provide evidence that spectrally stable devices can be obtained from RP-Cs system by forming a narrow intermediate-*m* domain distribution. The blue shifting of RP-FA and RP-MA EL spectra at high applied bias reveals the nonideal high-E_g (donor) to low-E_g (acceptor) domain ratio.

cation is used to curb formation of $m = \infty$ domains (Figure 1a). Toluene is introduced as an antisolvent during spin coating to promote fast nucleation rate, thus reducing the *m* domain distribution further. Three bromide salts of different A-site cations are compared, i.e., formamidinium bromide (FABr), methylammonium bromide (MABr), and cesium bromide (CsBr). Bulk solubility of these cations in a mixed DMF−DMSO cosolvent are found to be 10, 5, and 0.05 M respectively.

The capability of L cation: 4-phenyl-1-butylammonium cation ($C_6H_5(CH_2)_4NH_3^+$, referred to as PBA^+) to form $m = 1$ RP perovskite is confirmed by X-ray diffraction (XRD) analysis (Supplementary Note 1) with excitonic absorbance and photoluminescence (PL) peak features noted at 393 and 405 nm, respectively (Figure 1b). Difficulties in obtaining pure $m \geq 2$ RP phases from both homogeneous[20] and heterogeneous[21,22] nucleation methods are known, and therefore, for simplicity, ⟨*m*⟩ is used to represent the stoichiometric ratio in the precursor solution while *m* denotes the actual number of $[PbBr_6]$ layers present in the system. A-site cation variation does not appear to affect the roughness (~2 nm) and thickness (~30 nm) of these films (Figure S1).

The low-solubility A-site cation salt (Cs^+) is expected to limit formation of $m = 1$ and promote intermediate *m* domain formation due to the higher tendency to reach supersaturation. For the ⟨*m*⟩ = 2 system, employing high-solubility FA^+ results in a wide distribution of *m* domains as reflected in the RP-FA PL spectra where multiple peaks (405−525 nm) corresponding to $m = 1$ and *m* values approaching ∞ are observed (Figure 1c). Multiple PL peaks (405 to 474 nm) with narrow peak distribution, tentatively assigned to $m = 1$ and $m = 4$, are produced when less soluble MA^+ cation is utilized. Further narrowing of the PL peak distribution ranging from 438 to 463 nm is obtained when Cs^+, the cation with the lowest bulk solubility, is employed. These arise because of the favorable formation of $m = 1$ during the early nucleation stage, which reduces the L cation reservoir and facilitates growth of higher m domains (including ∞). This effect is evident for the highly soluble FA^+, where its slow incorporation into the low-m domain leads to the formation of higher-m domains and a larger PL peak distribution. For the low-solubility Cs system, the situation is reversed and rapid incorporation of Cs yields RP-Cs films with intermediate domains. Hence, we propose that the formation of low-m domains is kinetically favored during the initial stages of RP film growth because of strong van der Waals interaction between the L cations.[15,23] As the film growth proceeds, the A-site cation gets incorporated into the PBA^+ bilayer and forms higher-m domains[24] (Figure 1d). The large size and high solubility of FA^+ cation promote phase separation in the system as it is not readily incorporated for growth of low-m domains, unlike Cs^+ cation, where its small size and low solubility allow for easy incorporation into the low-m domains to form narrowly distributed intermediate-m domains.

In addition to compositional engineering, variations to nucleation and growth kinetics during film preparation also modulate the distribution of m domains in RP perovskites. Deposition methods involving slow and fast supersaturation processes were investigated by employing the conventional and antisolvent-assisted spin-coating procedures. The antisolvent technique induces fast supersaturation state, leading to smaller PL fwhm and lesser absorbance excitonic peaks due to the narrower m distribution across all systems regardless of the choice of antisolvent, A-site, and L cations (Figures 1b and S2; Supplementary Notes 2 and 3). This agrees with the LaMer burst model,[24,25] where a high rate of nucleation within a short period of time followed by slow rate of growth over a longer period promote the formation of monodispersed colloids and vice versa. Hence, aside from employing the compositional engineering strategy, antisolvent is also crucial to achieve a narrow m domain distribution.

To verify the RP perovskite formation mechanism, the absorbance spectra as a function of time on introduction of perovskite precursor solution into the antisolvent are monitored (Figure S3). As heterogeneous nucleation readily occurs at lower saturation as compared to the homogeneous system, the perovskite precursor solution is added to the antisolvent to mimic fast heterogeneous nucleation. The appearance of an excitonic absorbance peak confirms the formation of the RP perovskite. For RP-FA and RP-MA systems, the formation of $m = 2$ particles, as indicated by excitonic absorbance features at 433 and 429 nm, respectively, occurs instantaneously on addition of $\langle m \rangle = 2$ precursor solution. This can be explained by the stronger hydrogen bonding between the organic A-site cation (FA^+ and MA^+) and the inorganic octahedra.[26] Increasing the reaction time promotes particle growth as noted by the higher light scattering especially at longer wavelengths. On the other hand, as the reaction progresses, the absorbance shoulder at 450 nm becomes increasingly prominent, indicating higher amount of $m > 2$ nanoparticles forming in the RP-MA system after 40 s. In contrast, $m = 1$ particles with excitonic absorbance peak at 399 nm are the first to form for RP-Cs system despite Cs^+ (~0.05 M) lower bulk solubility limit as compared to PBA^+ (~5 M) in the DMF−DMSO cosolvent. With increasing reaction time, formation of higher-m nanoparticles becomes evident with signatures of assigned $m = 2$ (at 429 nm) and $m = 3$ (at 456 nm) observed after 40 s. This observation is consistent with the hypothesis that the formation of low-m nanoparticles is kinetically favored prior to growth of higher-m nanoparticles. The rate of growth for higher-m nanoparticles is faster for Cs^+ due to the smaller cation size and lower solubility.

Transient absorption (TA) spectroscopy, PL excitation spectra, and time-resolved photoluminescence (TRPL) data reveal the efficient energy cascade process from donor to acceptor domains in RP-Cs prepared with antisolvent processing (Supplementary Note 4), highlighting the need to completely eliminate $m \approx \infty$ domains for pure blue EL. An energy cascade process is also observed from TA spectra of RP-FA and RP-MA, with higher signal of high-m domains detected for RP-FA, followed by RP-MA, and RP-Cs, respectively (Supplementary Note 4). PeLEDs based on these systems, with standardized hole-transporting material (HTL) and electron-transporting material (ETL), are fabricated (Figure 2a). RP-Cs displays the lowest turn-on voltage ($V_{th} \approx 2.9$ V) indicating balanced charge injection among the three systems (Figure 2b). The energy cascade phenomenon is modulated by varying the donor-to-acceptor ratio, where efficient energy funneling results in an EQE boost while high donor-to-acceptor ratio leads to inefficient energy cascade and results in peak asymmetry or multiple emission peaks with low EQE.[27] Lower EQE and multiple EL peaks (Figures 2c,d and S4) are observed for both RP-FA (~0.002%) and RP-MA (~0.03%) systems because of the higher donor-to-acceptor ratio, which is in agreement with the PL data. On increasing applied bias, the EL spectra blue shifts, signifying incomplete energy transfer to the lowest E_g domain arising from insufficient acceptor concentration.[27] RP-Cs systems yield spectrally stable devices as the narrower m distribution offers an ideal donor-to-acceptor ratio guaranteeing high efficiency (~1.29%).[27] The poor spectral stability for devices prepared with conventional spin-coating process (Figure S5) further highlights the importance of the antisolvent technique for optimum donor-to-acceptor ratio. Hence, our study provides clear explanation for the domination of the Cs^+ system in most reports for blue RP-based PeLEDs (Table S1).

To vary the emission color, fine-tuning of PBA and Cs concentrations is pursued. Although $\langle m \rangle = 2$ was used, the majority of the emission comes from $m = 4$−5 with EL peak at 486 nm. In the regular $\langle m \rangle = 2$ solution with excess PBA, the PBA/Pb ratio is set at 1.5, whereas the PBA/Cs ratio is fixed at 3.3. We deduce that both PBA/Pb and PBA/Cs ratios play significant roles in controlling the proportion of intermediate-m domains. To attain deep blue emission (~460 nm), narrow spread of lower intermediate-m domains ($m = 3$−4) is achieved by slightly increasing the PBA/Pb precursor ratio. Meanwhile, although lowering Cs content enables tuning of PL emission, sufficient Cs^+ supply is required to maintain high PL intensity as acceptor domain concentration grows with increasing Cs incorporation into low-m domains. This prediction is in good agreement with the systematic blue shift of the PL peak and absorbance onset when the PBA/Pb ratio is increased up to 1.7 because of the preferred formation of lower intermediate-m domains (Figure S6). Increasing the PBA/Cs ratio to 5 results in less acceptor domains relative to the donor domains, which translates to multiple PL peaks regardless of the PBA/Pb ratio. Lowering the PBA/Cs ratio on

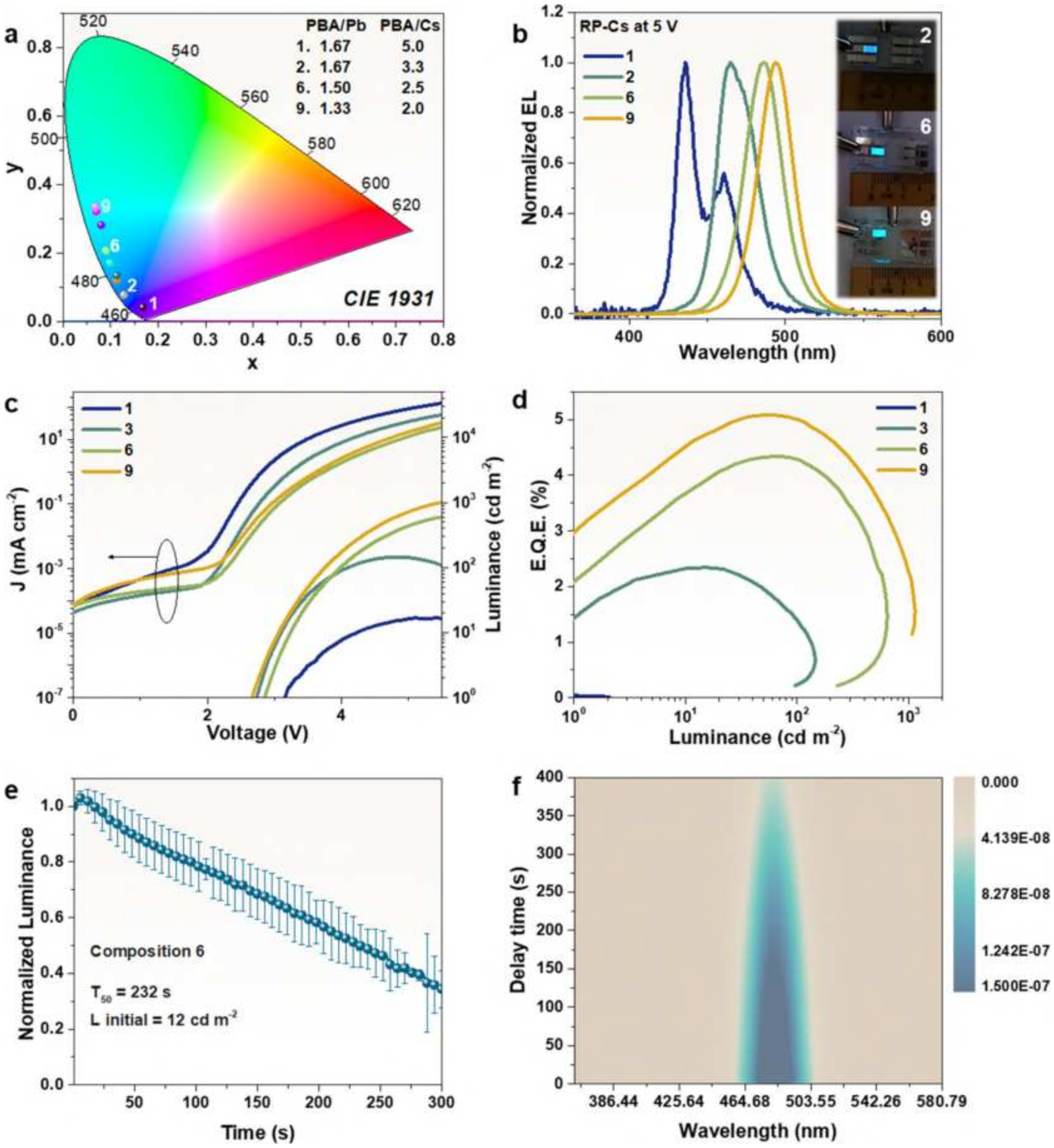

Figure 3. Spectrally tunable blue RP-Cs-based light-emitting diodes. The CIE coordinates of devices fabricated with various PBA/Pb and PBA/Cs ratios indicating the ease of tailoring the emission across the blue region (a). Normalized EL spectra with images of electrically driven devices fabricated from composition 2, 6, and 9 shown in inset (b), *J* and luminance curves as a function of voltage (c), and EQE versus luminance (d) of compositions 1, 2, 6, and 9 indicating that various high-efficiency PeLEDs with emissions spanning the blue region can be obtained from a single halide system. The time evolution of luminance (e) and EL spectral profile with increasing delay time (f) for composition 6, underlining the spectral stability of the emitter.

the other hand, slightly red shifts the PL and enhances the PL intensity of the film regardless of the PBA/Pb ratio because of the more efficient energy cascade with higher acceptor concentration (Figure S6).

Indeed, when both the PBA/Pb and PBA/Cs ratios are tuned, LEDs with EL emission ranging from ~437 to ~495 nm can be fabricated (Figure 3a). High V_{th}, low efficiency, and a blue shift of EL with increasing bias application are obtained for devices with PBA/Cs ratio of 5 because of the high donor-to-acceptor ratio (Figures S7 and S8). On lowering PBA/Cs ratio to 3.3 and below, the higher acceptor domain concentration results in the realization of spectrally stable EL despite high-bias application (Figure S8). Higher EQEs are achieved with lower PBA/Cs ratio regardless of the PBA/Pb ratio (Figure S7). Overall, maximum EQEs of 2.34, 4.34, and 5.08% are achieved with EL peak at 465, 486, and 493 nm, respectively (Figures 3b,d and S9 and Table S2). To date, this is the highest reported EQE for bicationic, pure bromide-based emissive blue RP perovskite LEDs (Table S1) with high efficiency and spectral stability maintained across the blue region. Spectral stability of device 6 is sustained throughout the lifetime measurement set at initial luminance of 12 and 100 cd·m^{-2} (Figures 3e,f and S10). Although operational stability is still low, the stable PL spectra and intensity measured for up to 30 min suggest that efficiency and stability of the device are limited by interfacial issues rather than material instability (Figure S11).

In summary, relying on a triptych of L and A cation concentrations, solubility limits of A cation, and nucleation kinetics, this report provides a methodology to tailor the perovskite structural landscape to deliver a narrow distribution ($m = 2-5$) of perovskite domains. This controlled distribution of RP domains is essential to ensure efficient blue emission. High concentrations of L cation are necessary to eliminate $m \approx \infty$ domains, whereas the role of the low-solubility A-site cation is to curb formation of undesired $m = 1$ domains. This structural landscape control has enabled record efficiencies of 2.34 and 5.08% corresponding to color stable deep blue and cyan, respectively, for bicationic, pure bromide-based emissive blue RP perovskite LEDs. The single-halide system utilized eliminates issues pertaining to halide segregation. This strategy is readily applicable to other L cation systems, leading to significant advancements in blue emission, and offers new avenues for CIE color spectrum tunability.

■ EXPERIMENTAL METHODS

Procedure for Preparation of the 4-Phenylbutylammonium Bromide Salt (PBABr, $C_6H_5(CH_2)_4NH_3Br$). To a round-bottom flask containing ethanol and 4-phenylbutylamine (PBA), cooled to 0 °C, was added a stoichiometric amount of concentrated hydrobromic acid. After the solution was stirred under the flow of argon (30 min), all volatiles were removed using a rotary evaporator. The fine powders thereby obtained were washed with copious amounts of diethyl ether, dried under vacuum (50 °C) overnight, and transferred into the glovebox. Isolated as a white solid (1.42 g; 92% yield). ^{1}H NMR (400 MHz, DMSO-d6): δ 7.82 (bs, 3 H, NH_3), 7.30−7.15 (m, 5 H, ArH), 2.81−2.78 (m, 2 H, CH_2), 2.60−2.57 (m, 2 H, CH_2), 1.65−1.51 (m, 4 H, CH_2). ^{13}C{^{1}H} NMR (100 MHz, DMSO-d6): δ 141.6, 128.3, 128.2, 125.8, 38.6, 34.5, 27.6, 26.5. ^{1}H and ^{13}C{^{1}H} NMR spectra of organic compounds were recorded in DMSO-d6 solution using a Bruker Avance 400 spectrometer. Chemical shift values (ppm) are referenced against residual protic solvent peaks.

Perovskite Film Formation. Depending on the choice of A-cation, mixtures of $PbBr_2$, ABr (A: $CH(NH_2)_2^+$, $CH_3NH_3^+$, Cs^+), and $C_6H_5(CH_2)_4NH_3Br$ in DMF: DMSO (64:36) solvents were used to produce the corresponding RP perovskite. To make $\langle m \rangle = 2$ solutions with excess $C_6H_5(CH_2)_4NH_3Br$, $PbBr_2$ (0.11 M) is mixed with ABr (0.05 M) and $C_6H_5(CH_2)_4NH_3Br$ (0.165 M) in which the PBA/Pb ratio and PBA/Cs ratio are set to 1.5 and 3.3, respectively. While keeping the $PbBr_2$ concentration fixed (0.11 M), the ratio of ABr and $C_6H_5(CH_2)_4NH_3Br$ are adjusted accordingly. Films were spin coated from various perovskite solutions at 5000 rpm for 30 s and dried at room temperature. If needed, antisolvent (i.e., toluene) is added 5 s from the initiation of each spin-coating process to induce fast nucleation. Both solution preparation and spin coating were done under inert argon environment.

Device Fabrication. Poly(3,4-ethylenedioxythiophene)polystyrenesulfonate (PEDOT:PSS, Al 4083) film was fabricated by spin coating at 4000 rpm for 60 s on top of indium tin oxide (ITO) coated glass. Substrates were then heated (200 °C, 40 s) to dry and transported inside the glovebox for perovskite deposition. The electron-transporting material ((1,3,5-triazine-2,4,6-triyl)tris(benzene-3,1- diyl))tris(diphenylphosphine oxide) (PO-T2T) (45 nm) and electrode (i.e., LiF (0.8 nm) and aluminum (100 nm)) were deposited via thermal evaporation method. Shadow masks are used during electrode evaporation to define a device area (8 mm^2).

Physical Characterization. The X-ray diffraction (XRD) patterns of the films were recorded using a Bruker D8 advance diffractometer with 0D LynxEYE detector. Topographical and cross-sectional images were captured by employing field effect scanning electron microscopy (FE-SEM, JEOL J7600F). Surface roughness measurement was conducted using atomic force microscopy (AFM, Asylum Research MFP-3D) under contact modes with Ti/Ir coated cantilevers (ASYELEC-01-R2, Asylum Research). Absorption and steady-state PL spectra were collected using a Shimadzu UV-3600 UV−vis−NIR spectrophotometer and a Horiba Fluoromax-4, respectively.

The transient absorption (TA) measurements were performed using a Helios spectrometer (Ultrafast Systems, LLC). The pump pulse was generated from by a 1 kHz regenerative amplifier [Coherent Legend (150 fs, 1 kHz, 800 nm)] and doubled via second harmonic generation (SHG) by a BBO crystal to obtain 400 nm laser pulses. The regenerative amplifier was seeded by a mode-locked Ti-sapphire oscillator (Coherent Vitesse, 80 MHz). The white light continuum probe beam (in the range from 410 to 750 nm) was generated by focusing a small portion (~10 μJ) of the fundamental 800 nm laser pulses into a 2 mm sapphire crystal, before filtering out the residual by using a 750 nm short-pass filter. Both pump and probe beam were focused onto the sample with 1/e^2 spot diameter of ~510 and ~200 μm, respectively. Meanwhile, the funneling time is estimated from the rise time of the bleaching signal ($\Delta R/R > 0$) of the bulk ($m > 3$) phases at 480 nm. Because of its ultrafast nature, this measured rise signal is the convolution between the exciton funneling time with our system response time (i.e., laser pulse width) of ~190 fs.

Time-resolved PL spectra were collected using a Picoquant PicoHarp 300 time-correlated single-photon counting (TCSPC) system integrated in a micro PL setup. The excitation source was a picosecond pulsed laser diode (Picoquant P-C-405B, $\lambda = 405$ nm, 40 MHz repetition rate). The luminescence signal was processed through an Acton SP-2300i monochromator coupled to an avalanche diode synchronized with the excitation laser via TCSPC electronics. The overall full width at half-maximum of the instrument response function is around 50 ps.

Device Characterization. The current−voltage responses of the devices were recorded using a Keithley 2612B instrument. An integrating sphere (OceanOptics FOIS-1) coupled with a calibrated spectrometer (OceanOptics QEPro) was used to collect the light emission output. To collect forward light emission only, devices were placed such that ITO glass is positioned at the opening of the integrating sphere. Absolute irradiance calibration was done by employing Ocean optics HL-3 Plus vis-NIR light source, which was calibrated using a process and documentation based on ISO 17025, IEC Guide 115, and JCGM100:2008 (GUM) protocols.

■ ASSOCIATED CONTENT

Supporting Information

The Supporting Information is available free of charge at https://pubs.acs.org/doi/10.1021/acsenergylett.0c00559.

Figures S1−S14, Tables S1 and S2, and Supplementary Notes 1−4 (PDF)

AUTHOR INFORMATION

Corresponding Authors

Subodh Mhaisalkar − *School of Materials Science and Engineering, Nanyang Technological University, 639798, Singapore;* orcid.org/0000-0002-9895-2426; Email: Subodh@ntu.edu.sg

Nripan Mathews − *School of Materials Science and Engineering, Nanyang Technological University, 639798, Singapore;* orcid.org/0000-0001-5234-0822; Email: Nripan@ntu.edu.sg

Authors

Natalia Yantara − *Energy Research Institute @ NTU, Nanyang Technological University, 637553, Singapore*

Nur Fadilah Jamaludin − *School of Materials Science and Engineering, Nanyang Technological University, 639798, Singapore*

Benny Febriansyah − *Energy Research Institute @ NTU, Nanyang Technological University, 637553, Singapore*

David Giovanni − *Division of Physics and Applied Physics, School of Physical and Mathematical Sciences, Nanyang Technological University, 637371, Singapore;* orcid.org/0000-0002-2764-5613

Annalisa Bruno − *Energy Research Institute @ NTU, Nanyang Technological University, 637553, Singapore;* orcid.org/0000-0002-6963-1682

Cesare Soci − *Division of Physics and Applied Physics, School of Physical and Mathematical Sciences, Nanyang Technological University, 637371, Singapore;* orcid.org/0000-0002-0149-9128

Tze Chien Sum − *Division of Physics and Applied Physics, School of Physical and Mathematical Sciences, Nanyang Technological University, 637371, Singapore;* orcid.org/0000-0003-4049-2719

Complete contact information is available at: https://pubs.acs.org/10.1021/acsenergylett.0c00559

Author Contributions

+N.Y. and N.F.J contributed equally to this work.

Notes

The authors declare no competing financial interest.

ACKNOWLEDGMENTS

This research was funded by National Research Foundation, Prime Minister's Office, Singapore under its Competitive Research Programme (CRP Award No. NRF-CRP14-2014-03), the Intra-CREATE Collaborative Grant (NRF2018-ITC001-001), and Office of Naval Research Global (ONRG-NICOP-N62909-17-1-2155). T.C.S. and D.G. acknowledge support from the Ministry of Education AcRF Tier 2 grant MOE2017-T2-1-001 and the NRF Investigatorship NRF-NRFI-2018-04. Dr. Sebastian Yongsen Quek is acknowledged for his contribution in absorbance versus time measurement.

REFERENCES

(1) Xing, G.; Mathews, N.; Sun, S.; Lim, S. S.; Lam, Y. M.; Grätzel, M.; Mhaisalkar, S.; Sum, T. C. Long-Range Balanced Electron- and Hole-Transport Lengths in Organic-Inorganic $CH_3NH_3PbI_3$. *Science* **2013**, *342* (6156), 344−347.

(2) Edri, E.; Kirmayer, S.; Mukhopadhyay, S.; Gartsman, K.; Hodes, G.; Cahen, D. Elucidating the Charge Carrier Separation and Working Mechanism of CH3NH3PbI(3-x)Cl(x) Perovskite Solar Cells. *Nat. Commun.* **2014**, *5*, 3461.

(3) Stranks, S. D.; Eperon, G. E.; Grancini, G.; Menelaou, C.; Alcocer, M. J. P.; Leijtens, T.; Herz, L. M.; Petrozza, A.; Snaith, H. J. Electron-Hole Diffusion Lengths Exceeding 1 Micrometer in an Organometal Trihalide Perovskite Absorber. *Science* **2013**, *342* (6156), 341−344.

(4) Xing, G.; Mathews, N.; Lim, S. S.; Yantara, N.; Liu, X.; Sabba, D.; Grätzel, M.; Mhaisalkar, S.; Sum, T. C. Low-Temperature Solution-Processed Wavelength-Tunable Perovskites for Lasing. *Nat. Mater.* **2014**, *13* (5), 476−480.

(5) Noh, J. H.; Im, S. H.; Heo, J. H.; Mandal, T. N.; Seok, S. Il. Chemical Management for Colorful, Efficient, and Stable Inorganic − Organic Hybrid Nanostructured Solar Cells. *Nano Lett.* **2013**, *13*, 1764−1769.

(6) Deschler, F.; Price, M.; Pathak, S.; Klintberg, L. E.; Jarausch, D. D.; Higler, R.; Hüttner, S.; Leijtens, T.; Stranks, S. D.; Snaith, H. J.; et al. High Photoluminescence Efficiency and Optically Pumped Lasing in Solution-Processed Mixed Halide Perovskite Semiconductors. *J. Phys. Chem. Lett.* **2014**, *5* (8), 1421.

(7) Tan, Z.-K.; Moghaddam, R. S.; Lai, M. L.; Docampo, P.; Higler, R.; Deschler, F.; Price, M.; Sadhanala, A.; Pazos, L. M.; Credgington, D.; et al. Bright Light-Emitting Diodes Based on Organometal Halide Perovskite. *Nat. Nanotechnol.* **2014**, *9*, 687−692.

(8) Chiba, T.; Hayashi, Y.; Ebe, H.; Hoshi, K.; Sato, J.; Sato, S.; Pu, Y. J.; Ohisa, S.; Kido, J. Anion-Exchange Red Perovskite Quantum Dots with Ammonium Iodine Salts for Highly Efficient Light-Emitting Devices. *Nat. Photonics* **2018**, *12* (11), 681−687.

(9) Lin, K.; Xing, J.; Quan, L. N.; de Arquer, F. P. G.; Gong, X.; Lu, J.; Xie, L.; Zhao, W.; Zhang, D.; Yan, C.; et al. Perovskite Light-Emitting Diodes with External Quantum Efficiency Exceeding 20 per Cent. *Nature* **2018**, *562* (7726), 245−248.

(10) Kim, J.; Chung, C. H.; Hong, K. H. Understanding of the Formation of Shallow Level Defects from the Intrinsic Defects of Lead Tri-Halide Perovskites. *Phys. Chem. Chem. Phys.* **2016**, *18* (39), 27143−27147.

(11) Kumawat, N. K.; Liu, X. K.; Kabra, D.; Gao, F. Blue Perovskite Light-Emitting Diodes: Progress, Challenges and Future Directions. *Nanoscale* **2019**, *11* (5), 2109−2120.

(12) Manser, J. S.; Christians, J. A.; Kamat, P. V. Intriguing Optoelectronic Properties of Metal Halide Perovskites. *Chem. Rev.* **2016**, *116* (21), 12956−13008.

(13) Saparov, B.; Mitzi, D. B. Organic-Inorganic Perovskites: Structural Versatility for Functional Materials Design. *Chem. Rev.* **2016**, *116* (7), 4558−4596.

(14) Cao, D. H.; Stoumpos, C. C.; Farha, O. K.; Hupp, J. T.; Kanatzidis, M. G. 2D Homologous Perovskites as Light-Absorbing Materials for Solar Cell Applications. *J. Am. Chem. Soc.* **2015**, *137* (24), 7843−7850.

(15) Xing, J.; Zhao, Y.; Askerka, M.; Quan, L. N.; Gong, X.; Zhao, W.; Zhao, J.; Tan, H.; Long, G.; Gao, L.; et al. Color-Stable Highly Luminescent Sky-Blue Perovskite Light-Emitting Diodes. *Nat. Commun.* **2018**, *9* (1), 1−8.

(16) Quan, L. N.; Zhao, Y.; García De Arquer, F. P.; Sabatini, R.; Walters, G.; Voznyy, O.; Comin, R.; Li, Y.; Fan, J. Z.; Tan, H.; et al. Tailoring the Energy Landscape in Quasi-2D Halide Perovskites Enables Efficient Green-Light Emission. *Nano Lett.* **2017**, *17* (6), 3701−3709.

(17) Yuan, M.; Quan, L. N.; Comin, R.; Walters, G.; Sabatini, R.; Voznyy, O.; Hoogland, S.; Zhao, Y.; Beauregard, E. M.; Kanjanaboos, P.; et al. Perovskite Energy Funnels for Efficient Light-Emitting Diodes. *Nat. Nanotechnol.* **2016**, *11* (10), 872−877.

(18) Jiang, Y.; Qin, C.; Cui, M.; He, T.; Liu, K.; Huang, Y.; Luo, M.; Zhang, L.; Xu, H.; Li, S.; et al. Spectra Stable Blue Perovskite Light-Emitting Diodes. *Nat. Commun.* **2019**, *10* (1), 1868.

(19) Liu, Y.; Cui, J.; Du, K.; Tian, H.; He, Z.; Zhou, Q.; Yang, Z.; Deng, Y.; Chen, D.; Zuo, X.; et al. Efficient Blue Light-Emitting Diodes Based on Quantum-Confined Bromide Perovskite Nanostructures. *Nat. Photonics* **2019**, *13*, 760.

(20) Oswald, I. W. H.; Koegel, A. A.; Neilson, J. R. General Synthesis Principles for Ruddlesden−Popper Hybrid Perovskite

Halides from a Dynamic Equilibrium. *Chem. Mater.* **2018**, *30*, 8606−8614.

(21) Hu, Y.; Spies, L. M.; Alonso-Álvarez, D.; Mocherla, P.; Jones, H.; Hanisch, J.; Bein, T.; Barnes, P. R. F.; Docampo, P. Identifying and Controlling Phase Purity in 2D Hybrid Perovskite Thin Films. *J. Mater. Chem. A* **2018**, *6* (44), 22215−22225.

(22) Quintero-Bermudez, R.; Gold-Parker, A.; Proppe, A. H.; Munir, R.; Yang, Z.; Kelley, S. O.; Amassian, A.; Toney, M. F.; Sargent, E. H. Compositional and Orientational Control in Metal Halide Perovskites of Reduced Dimensionality. *Nat. Mater.* **2018**, *17* (10), 900−907.

(23) Zhou, N.; Shen, Y.; Li, L.; Tan, S.; Liu, N.; Zheng, G.; Chen, Q.; Zhou, H. Exploration of Crystallization Kinetics in Quasi Two-Dimensional Perovskite and High Performance Solar Cells. *J. Am. Chem. Soc.* **2018**, *140* (1), 459−465.

(24) Liang, K.; Mitzi, D. B.; Prikas, M. T. Synthesis and Characterization of Perovskite Films Using Two-Step Dipping Technique. *Chem. Mater.* **1998**, *10* (1), 403−411.

(25) Chiang, C. H.; Wu, C. G. A Method for the Preparation of Highly Oriented $MAPbI_3$ Crystallites for High-Efficiency Perovskite Solar Cells to Achieve an 86% Fill Factor. *ACS Nano* **2018**, *12*, 10355−10364.

(26) Svane, K. L.; Forse, A. C.; Grey, C. P.; Kieslich, G.; Cheetham, A. K.; Walsh, A.; Butler, K. T. How Strong Is the Hydrogen Bond in Hybrid Perovskites? *J. Phys. Chem. Lett.* **2017**, *8* (24), 6154−6159.

(27) Yantara, N.; Bruno, A.; Iqbal, A.; Jamaludin, N. F.; Soci, C.; Mhaisalkar, S.; Mathews, N. Designing Efficient Energy Funneling Kinetics in Ruddlesden−Popper Perovskites for High-Performance Light-Emitting Diodes. *Adv. Mater.* **2018**, *30* (33), 1800818.